frontiers | Frontiers in Marine Science

TYPE Original Research
PUBLISHED 07 March 2025
DOI 10.3389/fmars.2025.1536339

OPEN ACCESS

EDITED BY
Li Li,
Zhejiang University, China

REVIEWED BY
Junliang Gao,
Jiangsu University of Science and Technology, China
Jingui Liu,
Guangdong Ocean University, China

*CORRESPONDENCE
Wenyun Guo
wyguo@shmtu.edu.cn

RECEIVED 28 November 2024
ACCEPTED 12 February 2025
PUBLISHED 07 March 2025

CITATION
Guo W, Zhang F, Ge J and Zhang H (2025) Tide-surge interaction and its impact on coastal inundation: a case study of super typhoon Meranti.
Front. Mar. Sci. 12:1536339.
doi: 10.3389/fmars.2025.1536339

Tide-surge interaction and its impact on coastal inundation: a case study of super typhoon Meranti

Wenyun Guo[1]*, Fenglin Zhang[1], Jianzhong Ge[2] and Hongsheng Zhang[1]

[1]College of Ocean Science and Engineering, Shanghai Maritime University, Shanghai, China, [2]State Key Laboratory of Estuarine and Coastal Research, East China Normal University, Shanghai, China

Typhoon-induced storm tides can cause severe coastal inundation hazards in low-lying lands. The extreme water levels can be significantly modified by the nonlinear tide-surge interactions. To explore the impact of these interactions on coastal inundation on Xiamen Bay and its adjacent low-lying coastal regions during Super Typhoon Meranti (1614), a series of numerical experiments utilizing a high-resolution FVCOM model were conducted. The results show that tide-surge interaction is extremely strong in Xiamen Bay, with relative intensity of 0.1 to astronomical tides and over 0.3 to the practical surges across most area of the bay. The nonlinear interaction tends to decrease the peak water levels across the bay but elevates peak surges in most parts of it. There are two peaks in the surges. The former peak occurs around mid-rising tide, and can mainly attribute to the nonlinear tide-surge interaction, while the latter mid-falling peak is resulted from the combined action of the strong wind and tide-surge interaction. The momentum balance analysis revealed that nonlinear transformations in local acceleration and advection terms are remarkable throughout the bay, and the nonlinear transformations in surface wind stress and bottom friction are significant in the shallow Jiulong River Estuary and the waters around Dadeng Island. During this storm, tide-surge interactions led to a significant reduction in inundation area, inundation depths, and inundation duration, by about 24%, 16%, and 10%, respectively. This study highlights the importance of considering tide-surge interactions in the assessment of coastal inundations risks.

KEYWORDS

tide-surge interaction, Xiamen Bay, coastal inundation, nonlinear terms, FVCOM

1 Introduction

Typhoon-induced coastal inundation is among the most severe natural hazards in coastal areas. It is expected to be exacerbated with global mean sea level rise, and typhoon intensifications in the warmer future (Aðalgeirsdóttir et al., 2021). In addition, the persistent coastal migration and urbanization are enhancing exposure to inundation,

which will result in higher damage and casualties (Zhang et al., 2018). The extreme water levels during typhoons are closely related to nonlinear interactions of surges, astronomical tides, waves, river discharge and so on (Arns et al., 2020; Gao et al., 2021; Johns et al., 1985; Xiao et al., 2021). But these interactions were not well captured in global assessment of extreme water levels and coastal inundation (Aðalgeirsdóttir et al., 2021; Arns et al., 2020). Therefore, it is of great significance to understanding the role of nonlinear interactions in extreme water levels and coastal inundations.

The nonlinear tide-surge interaction has been widely studied in recent decades (Idier et al., 2019; Proudman, 1955; Zhang et al., 2010). A positive surge tends to accelerate tidal propagation and advance the timing of high water, whereas a negative surge slows down tidal propagation (Prandle and Wolf, 1978; Rossiter, 1961). Thus, surge levels that coincide with rising tides tend to be higher, and surges near high tide tend to be lower (Prandle and Wolf, 1978; Zhang et al., 2017). Accordingly, a simple superposition method overestimates peak water levels, as studied by Johns et al. (1985) in the Bay of Bengal, by Tang et al. (1996) along the north Queensland coast of Australia, and by Antony et al. (2020) at the head of the Bay of Bengal.

The residual levels caused by the nonlinear tide-surge interaction can be significant. For example, during Typhoon Rammasun (1409), which struck the southern coast of China with sustained wind speed of nearly 70 m s-1, the nonlinear residual levels in Tieshan Bay, China, reached over 0.9 m (Yang et al., 2019). Significant nonlinear tide-surge interactions, which results in residuals of 0.2 m or greater, have been reported in many regions, including the North Sea (Horsburgh and Wilson, 2007), the Taiwan Strait (Liu et al., 2016; Zhang et al., 2010), the Bay of Bengal (Assalek and Yasuda, 2001), the Gulf of Mexico (Rego and Li, 2010), and along Australian coasts (Tang et al., 1996).

It has been well documented that tide-surge interaction mainly arises from three key nonlinear physical processes: (1) the nonlinear horizontal and vertical advection in the momentum equations, (2) the nonlinear bottom friction related to quadratic parametrization, (3) the shallow water effect arising from the tidal modulation of total water depth in both the continuity and momentum equations (Idier et al., 2019; Tang et al., 1996; Zhang et al., 2010). Nonlinear bottom friction always plays a predominant role in tide-surge interaction in shallow water areas with strong tidal currents (Idier et al., 2012; Zhang et al., 2017; Zheng et al., 2020). The alignment of strong tidal and storm-induced currents substantially increases the bed shear stress, which forces more surge residuals to generate stronger pressure gradient force (surface slope) to offset it (Idier et al., 2019). The shallow water effect becomes significant in cases of small tidal range in waters of less than 10 m deep, as demonstrated by Wolf (1981). Considering an idealized situation where the barotropic pressure is in equilibrium with the wind stress, a simple relationship can be derived whereby surge residuals are inversely proportional to the total water depth (Pugh, 1987). Strong winds during typhoons produce more surge in shallow waters, resulting in greater surge at low tide and reduced surge at high tide. Nonlinear advection tends to be much larger in the presence of complex bathymetries and coastlines, as indicated by Li (2006) and Li et al. (2008). This conclusion is further confirmed by comparing realistic and idealized simulations of the storm surge during Hurricane Rita along the Louisiana-Texa coast, which showed that the advection term was in the same order of the friction term in the realistic simulation, but five times smaller than the friction in the idealized simulations (Rego and Li, 2010).

Recent studies indicated that waves also can modulate the nonlinear tide-surge interactions. It can modulate surges through wave setup, wave-current interactions, and triggering resonance in local scales (Dong et al., 2023; Elahi et al., 2023; Gao et al., 2021; He et al., 2020). Li et al. (2022) indicated that wave can contribute 5% to the total surges in the macrotidal Hangzhou Bay. Whereas, in the Taiwan Strait, wave setup during typhoon Morakot contribute up to 24% of the total storm surges (Yu et al., 2017). Song et al. (2020) regarded that wave played an important role in the quarter-diurnal surges of the southwestern Bohai Bay, mainly through wave-current interactions. Wave may cause more significant influence to the surges in local waters. In the Yangshan Harbor, it contributed over 14% to peak surges (He et al., 2020). Waves also can cause resonance in harbors, resulting in significant modulations in surges (Dong et al., 2023; Gao et al., 2024).

Although the comprehensive understanding of characteristics and mechanisms of tide-surge interaction, knowledge of its role in coastal inundations are limited. Pinheiro et al. (2020) demonstrated that inundation patterns are sensitive to the tide-surge interaction through a model study in Ria de Aveiro lagoon. Lyddon et al. (2018) assessed the flood hazard in the Severn Estuary, and emphasized that the concurrence of tide and surge increased flood hazard throughout the estuary. Xiao et al. (2021) simulated coastal storm surges and inundations in the Delaware Bay Estuary during four historical hurricanes, and highlighted that the tide-surge interactions mainly influenced diurnal tides and increased the water level downstream.

The initial objective of this study is to synthetically explore the impact of tide-surge interaction on coastal inundation. We depict in detail the characteristics of tide-surge interaction and coastal inundation during a typical typhoon event in Xiamen Bay, a semi-enclosed bay in China. A high-resolution numerical model, which accounts for the complex dynamics of low-lying tidal flats, is established and applied to facilitate this study. The contributions of tide-surge interaction to inundation depth, inundation area, and inundation duration are estimated quantitatively.

2 Materials and methods

2.1 The Xiamen Bay and super typhoon Meranti (1614)

The macrotidal semi-enclosed Xiamen Bay is located on the southeastern coast of mainland China (Figure 1), connecting the Jiulong River Estuary with the Taiwan Strait. The many islands in the bay, including Xiamen Island, Dajinmen Island and Xiaojinmen Island, lead to extreme complexity in the coastlines and topography. The tidal range at the Xiamen gauge station (Figure 1) ranges from 1.0 m to over 6.4 m, with an average value of 4.0 m. Tidal range tends to increase roughly from the mouth towards the head of the bay spatially.

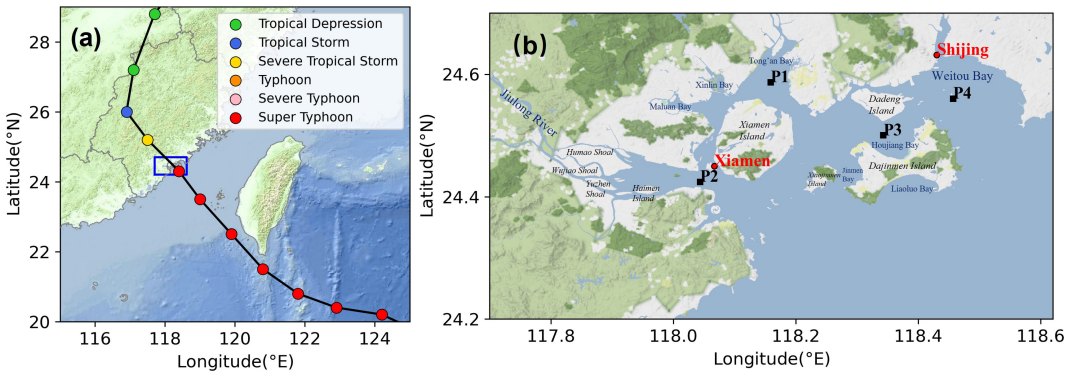

FIGURE 1
(a) The 6-hourly track and intensity of Super Typhoon Meranti (1614), which make landfall at Xiamen Bay in September 2016. The blue box indicates the zoomed-in area shown in **(b)**. **(b)** Map of Xiamen Bay and locations of tidal gauges (red bullets). The four black squares indicate the representative stations for result analysis.

The excellent navigation conditions promote Xiamen as an important sub-provincial city for China. Statistics show that Xiamen had 5.16 million permanent residents and produced CNY 634.8 billion in Gross Domestic Product in 2020. The dense population and high economic output highlight the significance of understanding the storm surges and their impact on coastal flooding in this region.

The Xiamen Bay is seriously affected by typhoons. According to the statistical analysis of surges from 1959 to 2012, there were 145 typhoons that had significant impacts (surge level > 0.5 m) on this region, averaging 2.7 typhoons per year (Miao et al., 2022). Though it is well protected by high-level coastal defenses, extensive coastal flooding can still be brought about by typhoons. For example, typhoon Dujuan (1521) inundated several coastal low-lying areas and wharfs on Xiamen Island (Yuan et al., 2022). According to long-term observed water levels, the Xiamen is among one of the regions with extremely significant tide-surge interactions along the coast of China (Feng et al., 2019). However, to the best of our knowledge, detail studies of the tide-surge interaction in Xiamen Bay have not been reported, and its impact on local inundation.

Super Typhoon Meranti (1614) was the strongest typhoon to strike Fujian Province, China since 1949. It formed in the western North Pacific Ocean on 10 September 2016, then traveled northwest and passed through the Luzon Strait, coming close to Taiwan Island at 05:00 a.m. on 13 September. It made landfall in Xiamen, China at about 03:05 a.m. on 15 September (Figure 1). At the time of landfall, the sustained maximum wind speed was about 48 m s-1 and the minimum central pressure was about 945 hPa, classifying it as a severe typhoon. Meranti caused economic losses of over CNY 280 million and destroyed 106 ships and 650,000 trees in Xiamen. The observed maximum surges in Xiamen Bay were over 1.0 m.

2.2 Model configuration

The Finite-Volume Community Ocean Model (FVCOM, version 4.1) (Chen et al., 2003; 2013) is employed to investigate the tide-surge interaction during Typhoon Meranti in Xiamen Bay. FVCOM is a prognostic, free-surface, three-dimensional model based on primitive equations for coastal oceans. The non-overlapped triangular mesh that FVCOM adopts in the horizontal plane can accurately fit the irregular coastlines. The triangular mesh also offers convenience of refining the mesh in areas of interest. FVCOM offers multiple vertical coordinate systems, including the traditional z and sigma coordinates, as well as the generalized terrain-following sigma coordinate (s-coordinate).

The surface wind stress and bottom friction stress are parameterized by a quadratic drag law:

$$(\tau_{sx}, \tau_{sy}) = \rho_a C_s \sqrt{U_{10}^2 + V_{10}^2}(U_{10}, V_{10}) \quad (1)$$

$$(\tau_{bx}, \tau_{by}) = \rho_a C_d \sqrt{u^2 + v^2}(u, v) \quad (2)$$

In Equations 1 and 2, ρ_a is the air density, C_s and C_d are the wind drag coefficient and the bottom drag coefficient, respectively; (U_{10}, V_{10}) represent the wind speed components at 10 m height above the sea surface. (u, v) are the water current components at the bottom layer in the east and north directions, respectively.

The wind drag coefficient C_s is a function of the sea surface roughness. It increases monotonously with wind speed during calm weather. However, complexity emerges during high-wind conditions, and the specific relationship remains unfixed (Peng and Li, 2015). Thus, a simple linear function that levels off at high wind speed, as originated by Large and Pond (1981), is adopted in this study:

$$C_s = \begin{cases} 0.0012, & |\mathbf{V}_{10}| < 11 \\ 10^{-3}(0.49 + 0.065|\mathbf{V}_{10}|), & 11 \le |\mathbf{V}_{10}| \le 25 \\ 10^{-3}(0.49 + 0.065 \times 25), & 25 < |\mathbf{V}_{10}| \end{cases} \quad (3)$$

In Equation 3, $|\mathbf{V}_{10}| = \sqrt{U_{10}^2 + V_{10}^2}$ is the magnitude of wind speed.

The bottom drag coefficient C_d is determined by matching a logarithmic bottom layer to the model at height of z_{ab} above the seabed:

$$C_d = max\left(\frac{\kappa^2}{ln(z_{ab}/z_0)^2}, 0.0025\right) \quad (4)$$

where $\kappa = 0.4$ is the von Karman constant, z_{ab} is the distance from the seabed to the position of u and v, and z_0 in Equation 4 is the bottom roughness parameter, and is set a constant value of 0.0002 in this study.

The model domain for Xiamen Bay encompasses the entire Taiwan Strait and extends 1000 km seaward into the Pacific Ocean (Figure 2). The large-scale coverage helps to account for possible far-field effects resulting from typhoon formation and its approaching (Huang et al., 2022; Thomas et al., 2022). In Xiamen Bay, the model domain extends landward, covering all low-lying lands lower than 20 m. Seawalls in Xiamen Bay have also been incorporated into our model. The model features a resolution of 200 m within Xiamen Bay and approximately 80 km at the open boundary. The model utilizes 4 vertical sigma layers.

The topography used in the model integrates 1 arc-minute ETOPO1 data (Amante and Eakins, 2009) for offshore region, a large number of high-resolution (100 – 2000 m) naval electronic nautical charts in coastal areas, and a 10-m-resolution DEM dataset of Xiamen Bay for low-lying lands. The model is driven by tidal forcing in the open boundary and wind forcing at the sea surface. Eight tidal constituents (M_2, S_2, N_2, K_2, K_1, O_1, P_1, and Q_1) derived from the latest released satellite-assimilated tidal model TPXO9-atlas (Egbert and Erofeeva, 2002) are used to generate tidal water levels at the open boundary. Daily river discharge summated from stations Punan and Zhengdian is assigned at the Jiulong River boundary. The surface wind forcing is a combination of a reanalysis background wind product, namely, the hourly ERA5 dataset (Hersbach et al., 2020) from the European Centre for Medium-Range Weather Forecasts, with an asymmetric parametric typhoon field. This field is a superposition of a circular symmetric typhoon wind field, as proposed by Fujita (1952), and a moving wind field, as recommended by Miyazaki (1962). A detailed description of the blended typhoon wind can be found in Guo et al. (2023).

2.3 Numerical experiments

Three numerical experiments have been conducted to investigate the nonlinear tide-surge interaction in the Xiamen Bay and explore its impact on coastal inundation:

1. Full run (Run-F), which is the realistic simulation driven by both tidal forcing at the open boundary and the blended typhoon wind field at the sea surface. The resultant water level from this experiment is the storm tide (ζ_{TS}).
2. Tide-only run (Run-T), which is driven solely by tidal forcing at the open boundary. The resultant water level is the pure astronomical tide (ζ_T).
3. Storm-only run (Run-S), which is driven solely by the blended typhoon wind field at the sea surface. The resultant water level is the pure storm surge (ζ_S).

Thus, the water level due to tide-surge interaction (ζ_I) can be calculated as $\zeta_I = \zeta_{TS} - \zeta_T - \zeta_S$. Furthermore, the summation of the pure astronomical tide and pure storm surge ($\zeta_T + \zeta_S$) is referred to as the virtual storm tide in this study. In practice, storm surges are typically evaluated by subtracting the astronomical tides from the observed tidal levels (Horsburgh and Wilson, 2007; Zhang et al., 2010). This surge level is termed the practical surge (ζ_{SI}) in this study, such that $\zeta_{SI} = \zeta_{TS} - \zeta_T$.

All the experiments started on 5 September 2016, and ended at 20 September. The experiments were initialized from a state of rest (i.e., zero water levels and velocities) and spun up for the first 7 days. A widely-used split-mode technique is applied in these experiments, with a 1-second internal time step and a 0.2-second external time

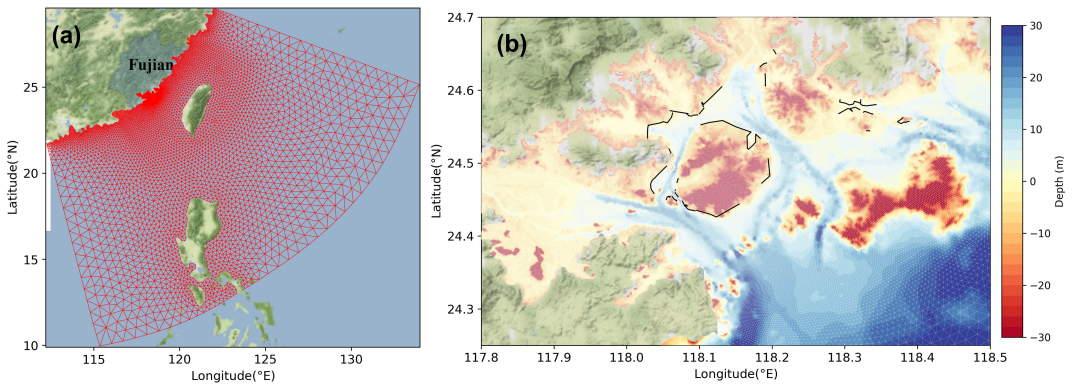

FIGURE 2
(a) Unstructured triangular mesh for Xiamen Bay used in this study. **(b)** zoomed-in view in Xiamen Bay. Colors denote the topography. Note that the mesh covers the low-lying land in Xiamen Bay.

step. To capture finer details of the storm tides and storm surges, the results are output at 10-minute intervals.

2.4 Quantifying relative intensity of tide-surge interaction to storm tides

The absolute intensity of tide-surge interaction can be represented by the maximum value of residual ζ_I. Following the studies by Rego and Li (2010) and Zheng et al. (2020), the relative intensity of tide-surge interaction compared to the pure astronomical tide can be defined as

$$I_T = \frac{RMS(\zeta_I)}{RMS(\zeta_T)} \tag{5}$$

where the RMS(ζ_*) = $\left[\frac{1}{T}\int_0^T \zeta_*^2(t)dt\right]^{\frac{1}{2}}$ is the root-mean-square (RMS) of ζ_*. Similarly, the relative intensity of tide-surge interaction compared to the practical surge can be defined as

$$I_{SI} = \frac{RMS(\zeta_I)}{RMS(\zeta_{SI})} \tag{6}$$

3 Results

3.1 Model Validation

Three error skills, namely, root-mean-square error (RMSE), relative error (RE) related to the varying range, and model skill (MS) metrics are utilized to quantify the model's performance on storm tides and surges. The RMSE denotes the average deviation of the model results from the observations and is calculated as

$$\mathrm{RMSE} = \sqrt{\sum_{i=1}^{N}(X_m^i - X_o^i)^2/N}, \tag{7}$$

where X_m^i and X_o^i are the model simulation and observed data at time i, respectively; N is the number of observed records used for the comparison. The RE evaluates the relative error of model results, and is given by

$$\mathrm{RE} = \frac{\sum_1^N |X_m^i - X_o^i|/N}{TR_o} \times 100\,\%, \tag{8}$$

where XR_o is the varying range of observations. The MS is a dimensionless quantity proposed by Willmott (1981), which is widely-used in quantifying the consistency between two oscillatory data sets, and is calculated as

$$\mathrm{MS} = 1 - \frac{\sum_{i=1}^{N}(X_m^i - X_o^i)^2}{\sum_{i=1}^{N}\left(\left|X_o^i - \overline{X_o}\right|^2 + \left|X_m^i - \overline{X_m}\right|^2\right)}, \tag{9}$$

where the overbar represents the mean values. The result is considered highly reliable when MS > 0.5.

Astronomical tidal data from the tidal tables at Xiamen and Shijing tidal gauges (Figure 1) were collected for the validation of astronomical tides. Figure 3 represents the comparison for the period of 10-31 August 2020. The error skills calculated by Equations 7–9 are also labelled in Figure 3. The RMSE values at the two stations are 0.22 and 0.16 m, respectively. The REs and MSs are less than 3.0% and greater than 0.98, respectively. These high skills suggest that the model can provide highly reliable predictions of astronomical tides.

The storm tides and surges recorded by the two tidal gauges during Typhoon Meranti were collected for further validation of the model. The results are presented in Figure 4. Typhoon Meranti significantly elevated tidal levels in Xiamen Bay. The observed

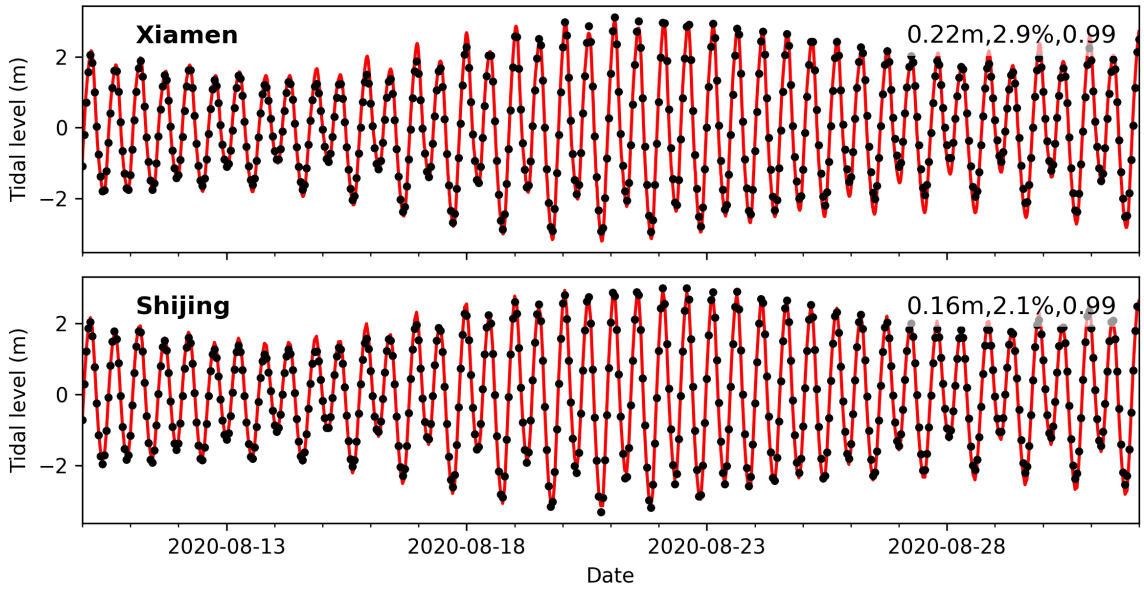

FIGURE 3
Comparison of astronomical tides between model results (red lines) and tidal tables (black dots) at tidal gauges Xiamen and Shijing. The RMSE, RE, and MS values are labeled.

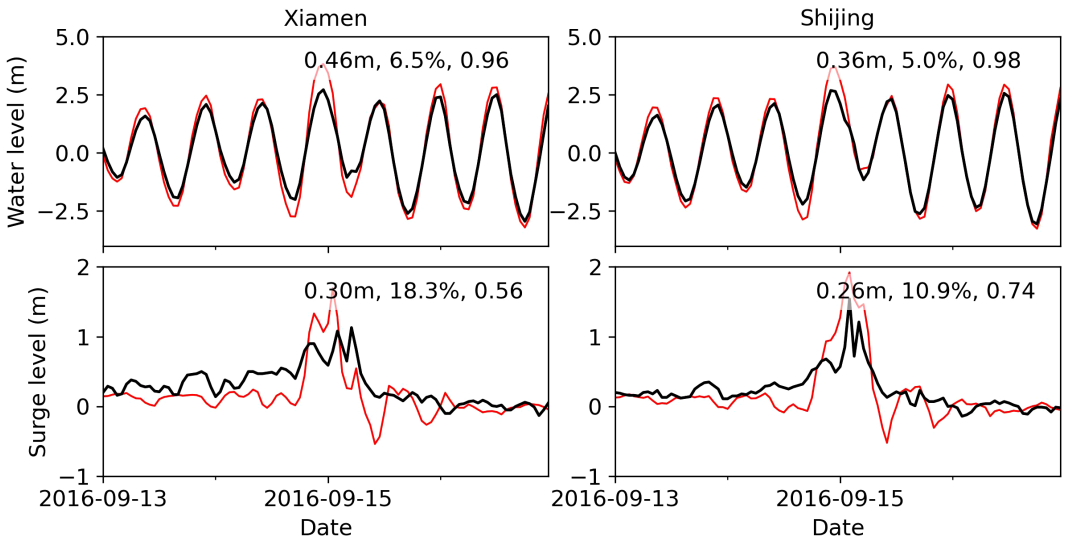

FIGURE 4
Comparison of storm tides and surges between model results (red lines) and observations (black lines) at tidal gauges Xiamen and Shijing. The RMSE, RE, and MS values are labeled.

surges at the Xiamen and Shijing tidal gauges reached their maximum (1.13m and 1.54m, respectively) at 05:00 and 02:00 AM on 15 September, respectively, coinciding closely with the time of landfall. Interestingly, the surge at Xiamen exhibited a double-peak pattern, reaching an initial peak (1.08m) at 02:00, then drop rapidly, and subsequently rising quickly to its maximum at 05:00. Similar phenomenon is observed at the Guangchong and Xipaotai tidal gauges in the Pearl River Estuary during Typhoon Hato (1713) (Zheng et al., 2020). They attributed this phenomenon to the rapid change in wind direction associated with the proximity of the station locations to the typhoon center. However, our research indicates that tide-surge interaction plays an important role in the occurrence of the double peaks in the observed surge.

As shown in Figure 4, although the skill of the model in reproducing storm tides during Typhoon Meranti is somewhat lower than that for astronomical tides, our model still reproduces the storm tides and surges in high credibility. The REs for the storm tides are less than 6.0% and the MSs are greater than 0.96. As for the surges, the RMSEs are less than 0.25 m, and the MSs are higher than 0.59. Additionally, our model successfully captures the double-peak pattern of the storm surge observed at the Xiamen tidal gauge.

3.2 Tide-surge Interaction

The modelled maxima of storm tides (ζ_{TS}) from Run-F in Xiamen Bay during Typhoon Meranti (1614) are displayed in Figure 5a. It is evident that the maximal storm tides are small (about 3.0 m) in the Taiwan Strait, but significantly high in Xiamen Bay. Especially in Jiulong River Estuary, east of Dajinmen Island, and north of Dadeng Island, the storm tides can nearly reach 5.0 m. The summation of pure astronomical tides (ζ_T) from Run-T and pure storm surges (ζ_S) from Run-S can be regarded as virtual storm tides without tide-surge interactions. The maxima of the virtual storm tides are shown in Figure 5b. Its spatial pattern is very similar to Figure 5a, but with apparent higher values. The maximal virtual storm tides can reach 4.5 m to the west of Xiamen Island and in the Houjiang Bay. Their differences presented in Figure 5c show that the virtual storm tides are higher than storm tides in the whole Xiamen Bay, except for some extremely shallow positions, where they can be easily flooded by storm tide but hardly to be affected by pure astronomical tide or pure storm surge. The differences represent the influence of the tide-surge interactions on peak water levels. Figure 5c shows that these influences are nearly spatially uniform. Nonlinear tide-surge interactions can reduce peak water levels in Xiamen Bay by an average of ~0.31 m. The reduced levels are relatively higher in the Jiulong River Estuary (~0.40 m), the Houjiang Bay (~0.40 m), and in the head of Weitou Bay (~0.33 m). This result demonstrates that nonlinear tide-surge interactions play a significant role in mitigating peak water levels across Xiamen Bay during Typhoon Meranti (1614).

The practical surge ζ_{SI} is calculated by subtracting the pure astronomical tide (ζ_T from Run-T) from the total storm tide (ζ_{TS} from Run-F). Figure 5d illustrates the spatial distribution of maximal practical surges. Maximal practical surges are relatively low to the southeast of Xiamen Island, and high in the Jiulong River Estuary, to the west of Xiamen Island, and in Weitou Bay. The spatial distribution of maximal pure storm surges (Figure 5e) also exhibits a similar spatial pattern with the maximal practical surges. Nevertheless, slight differences exist between them. These differences are notable to the east of Dajinmen Island and in the Jiulong River Estuary, where maximal pure surges are significantly higher. Figure 5f displays their differences, revealing that storm surge modulation by nonlinear tide-surge interaction is highly localized and varying spatially. The peak surges in Weitou Bay, around Dadeng Island, and in Tong'an Bay are elevated due to nonlinear tide-surge interaction. However, peak surges in the Jiulong River Estuary and south of Xiamen Island are reduced by the nonlinear tide-surge interaction. Similar results that peak surge

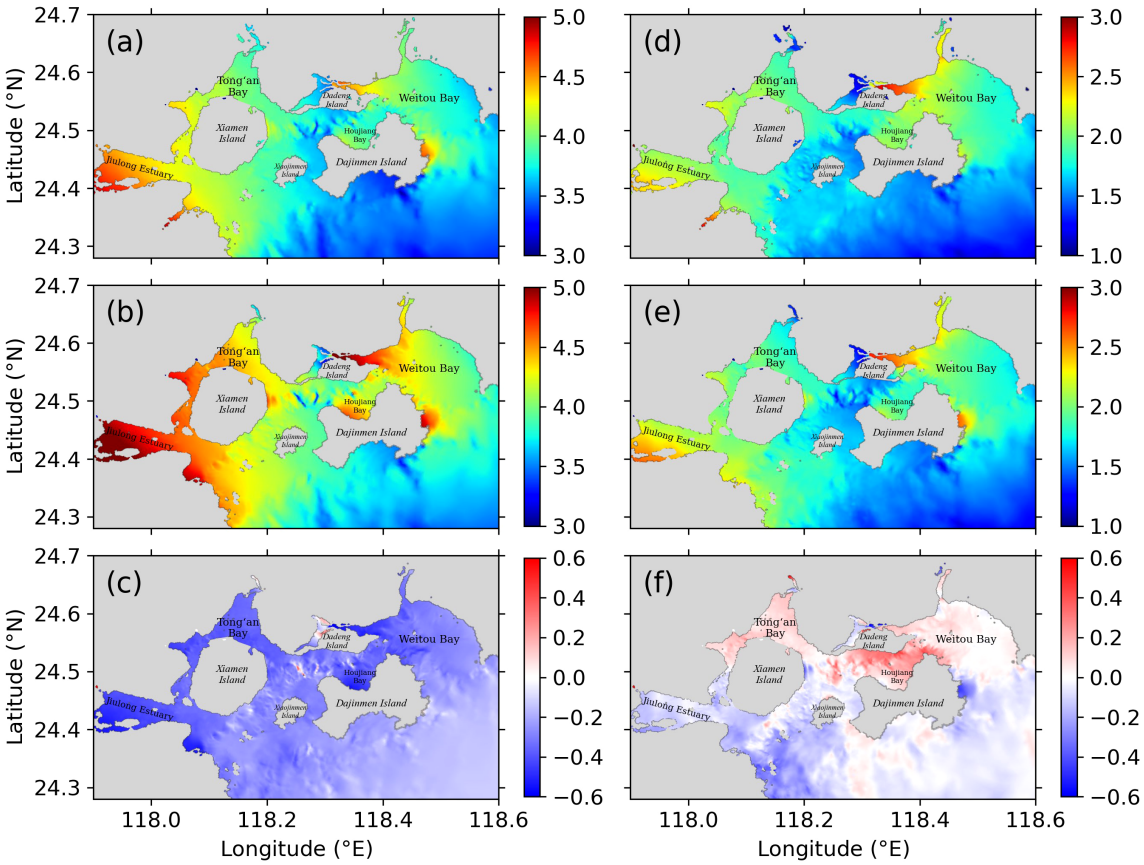

FIGURE 5
Spatial distribution of **(a)** maximum of ζ_{TS}, **(b)** maximum of $\zeta_T + \zeta_S$ and **(c)** the difference between the maximum of ζ_{TS} and $\zeta_T + \zeta_S$(i.e., MAX(ζ_{TS}) - MAX ($\zeta_T + \zeta_S$)); **(d)** maximum of ζ_{SI}, **(e)** maximum of ζ_S and **(f)** the difference between the maximum of ζ_{SI} and ζ_S(i.e., MAX(ζ_{SI}) - MAX(ζ_S)).

levels can be either elevated or reduced by tide-surge interaction are also found in the Solent tidal regime (Quinn et al., 2012), and in Pearl River Estuary (Zheng et al., 2020). Changes in peak surges induced by tide-surge interaction are significantly smaller than those in peak water levels induced by the same mechanism. The average change in peak surge levels is approximately 0.15 m around Dadeng Island, where exhibits a strongest change in peak surges.

Four representative stations (Figure 1b) in Tong'an Bay (P1), Jiulong River Estuary (P2), Houjiang Bay (P3) and Weitou Bay (P4) are selected to analyze the temporal characteristics of residual water levels resulting from tide-surge interactions. As shown in Figure 6, significant practical surges, pure surges and residuals due to tide-surge interactions occur within the 24-hour period centered on 00:00 a.m. on 15 September, and are negligible before and after Typhoon Meranti (1614) passes. There are more temporal variabilities in practical surges than pure surges during the storm. The pure surges increase and then decrease monotonically. However, practical surges experience a significant drop during high tide. Thus, a double-peak phenomenon emerges in the practical surge time series. Similar results have been reported in other regions, such as the Louisiana-Texas coast (Rego and Li, 2010), the east coast of Leizhou Peninsula, China (Zhang et al., 2017), and the Pearl River Estuary (Zheng et al., 2020).

The surge drop in high tide reflects the modulatory effect of the tidal forces, resulting in a trough in the tide-surge interaction residuals (ζ_I). Figure 6 also indicates two peaks in $\zeta_I$during mid-rising tide and mid-falling tide, especially at P1 of Tong'an Bay and P2 of Jiulong River Estuary. This suggests the presence of a two-peaks feature in the nonlinear residuals $\zeta_I$during the storm. The intensities of the oscillations in the residuals $\zeta_I$vary significantly among the different locations. The ζ_I oscillations manifest with greater strength in Tong'an Bay (P1) and Jiulong River Estuary (P2), and with less strength in Houjiang Bay (P3) and Weitou Bay (P4).

Given the concerns regarding the maximum water levels and surges during a storm, examining the maximum values of ζ_I is particularly important (Horsburgh and Wilson, 2007; Zhang et al., 2017). As demonstrated by Figure 7a, the maximum values of ζ_I exhibit a spatial pattern with larger magnitudes on the inland side and smaller ones at the bay entrance. They exceed 0.5 m at locations such as the Jiulong River Estuary, the western side of Xiamen Island, most of Tong'an Bay, and the head of Weitou Bay. The remarkable periodicity in ζ_I, as suggested by Figure 6, further underscores the value of calculating the root-mean-square (RMS) values to assess the average intensity of ζ_I during storms. Figure 7b shows that the RMS values of ζ_I mainly range from 0.1 to 0.3 m in Xiamen Bay, with higher values in the Jiulong River Estuary and Tong'an Bay.

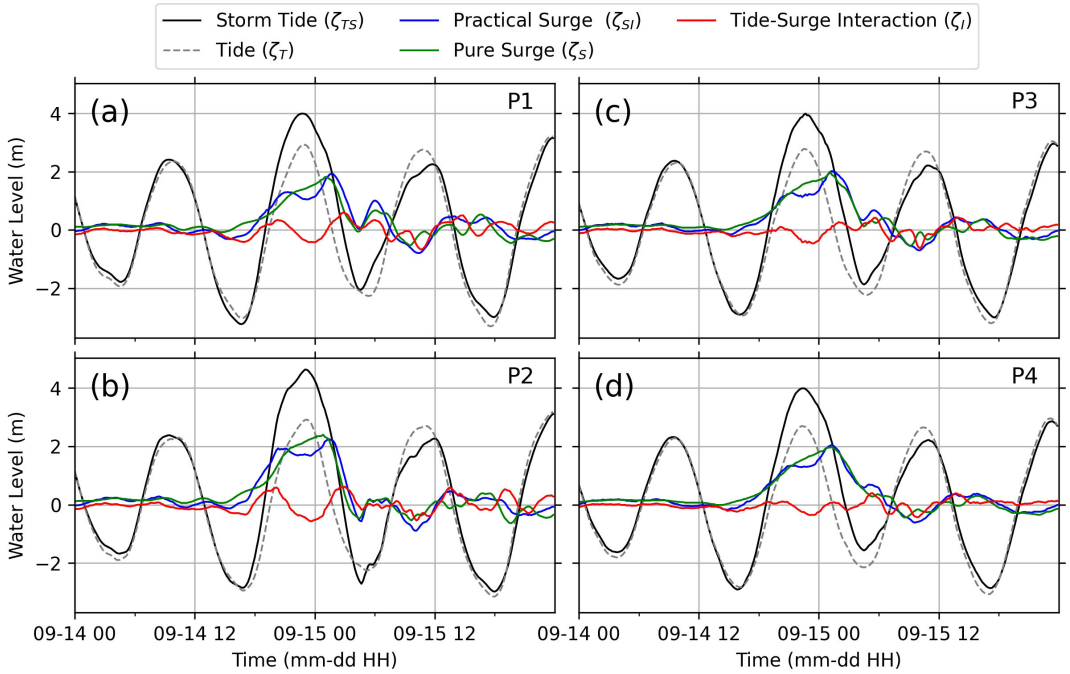

FIGURE 6
Time series of storm tides (ζ_{TS}, black solid lines), pure astronomical tides (ζ_T, black dashed lines), practical surges (ζ_{SI}, blue lines), pure surges (ζ_S, green line), and residual water levels due to the tide-surge interaction (ζ_I, red lines) at **(a)** P1, **(b)** P2, **(c)** P3 and **(d)** P4, which positions are indicated in Figure 1a.

Equations 5, 6 can assess the relative intensity of tide-surge interactions compared to astronomical tides and practical surges, respectively. The results of these assessments are displayed in Figures 7c, d. Due to the large tidal ranges in Xiamen Bay, the relative intensities of ζ_I compared to tides are small, approximately 0.10. In contrast, these intensities are relatively large, approximately 0.13, in Tong'an Bay and Jiulong River Estuary. However, the relative intensities of ζ_I compared to surges are significantly higher. These values exceed 0.2 across most of Xiamen Bay, and can reach up to 0.4 in Tong'an Bay, and to both the western and

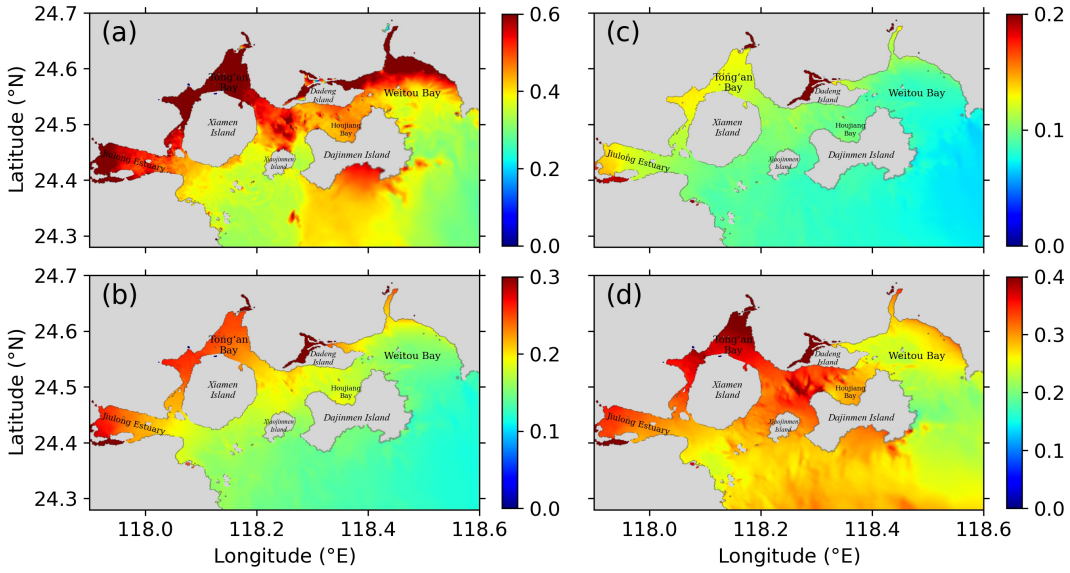

FIGURE 7
Spatial distribution of **(a)** maximum of residual water levels (unit: m) due to the tide-surge interaction (ζ_I), **(b)** RMS of ζ_I (unit: m), **(c)** the relative intensity of $\zeta_I$to $\zeta_T(I_T)$, and **(d)** the relative intensity of $\zeta_I$to$\zeta_{SI}(I_{SI})$. Note different scales of colorbars apply.

eastern sides of Xiamen Island. These results demonstrate the significant importance of tide-surge interaction in the surges observed in Xiamen Bay.

3.3 Coastal inundation and influence of tide-surge interaction

Coastal inundation during storms, such as Typhoon Meranti (1614), can lead to significant losses and even casualties due to extensive flooding. Our model results indicate that Typhoon Meranti (1614) can result in a considerable inundation in Xiamen Bay, with the maximum extent reaching approximately 210 km^2 (as shown in Figure 8a). A significant portion of this inundation, accounting for 61% of the affected area, occurred along the coastline of Weitou Bay and around Dadeng Island. Furthermore, the inundation depths were notably severe, with the maximum depth reaching about 4.8 meters and an average depth of ~3.1 meters.

The inundation area without tide-surge interactions is retrieved by applying a bathtub method to the virtual storm tides (ζ_T+ ζ_S). This method identifies inundation by checking if a grid node and at least one of its geometrically adjacent nodes are both inundated and hydraulically connected. Our findings, depicted in Figure 8b, reveal that in the absence of tide-surge interactions, the inundation area will significantly increase to ~260 km^2, i.e., an increase of about 50 km^2 or 24%. Notably, seawater will invade Xinglin Bay and Maluan Bay, areas not typically inundated when tide-surge interactions are considered, resulting deeper inundation levels (as a comparison between Figures 8a, b). This effect is particularly pronounced at the head of Weitou Bay, where the average inundation depth rises to ~3.6 m, marking an increase of 0.5 m (16%).

Whereas, their difference (Figure 8c) exhibits variabilities in space. Changes of inundation depth induced by tide-surge interaction do not decrease in the whole Xiamen Bay, but express a trend of magnification in some shallow corner zones, such as at east of Dadeng Island, and at head of Tong'an Bay.

Inundation duration is also among the key factors in assessing flood damage. The longer an area remains flooded, the greater the potential economic losses, particularly relating to the disruption of vital services such as electricity, transportation, and water treatment (Cruse, 2020; Feng et al., 2017; Pyatkova et al., 2019; Wagnaar, 2012). As depicted in Figure 8d, prolonged periods of inundation are notable around Dadeng Island, in Tong'an Bay, as well as at the

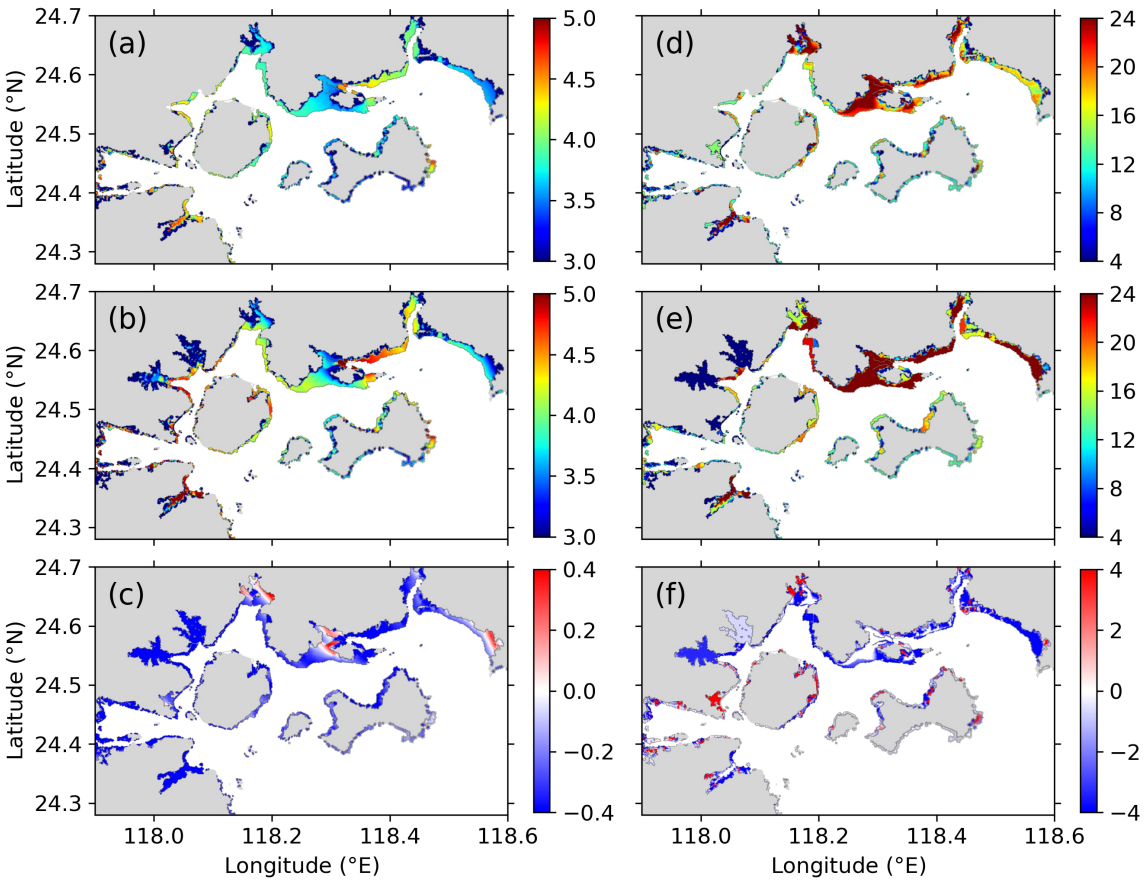

FIGURE 8
Spatial distribution of maximal inundation depths (unit: m) of **(a)** Run-F, **(b)** that deducted from the summation of Run-T and Run-S, and **(c)** their difference. Spatial distribution of inundation duration (unit: h) of **(d)** Run-F, **(e)** that deducted the summation of Run-T and Run-S, and **(f)** their difference. Inundation areas with height > 0.0 m are drawn.

head of Weitou Bay. When tide-surge interactions are not present, the inundation durations tend to lengthen in most affected areas, as shown in Figure 8e.

However, as we can see from the differences presented in Figure 8f, the impact of tide-surge interactions on the inundation durations is not uniform across all regions. In some coastal corners, the interaction may substantially decrease the inundation durations. On average, the inundation lasts for 15.1 hours when tide-surge interaction is considered and increases to 16.6 hours in its absence, suggesting that tide-surge interactions have the potential to reduce inundation duration by about 10%. These findings reveal a complex and spatially diverse relationship between tide-surge interactions and coastal inundation duration, emphasizing the need for detailed local analyses in flood risk management strategies.

The large tidal range in the Xiamen Bay implies that most of the low-lying lands with elevations below 3.0 m are routinely subjected to inundation due to astronomical tides. This periodic flooding reduces the urgency of focusing on these areas when planning flood defense efforts. Consequently, our analysis prioritizes land above this elevation, as shown in Figure 9. The timeseries data highlights that the interaction between tides and storm surges can have a profound effect on reducing the extent of flooding, particularly between 21:00 on the 14th and 01:00 on the 15th. At these times, the inundation area can be halved, offering significant protection and potentially lowering the impact of flood damage. Notably, during the peak of the inundation, this effect is even more pronounced, which is a key insight for flood mitigation strategies. However, the analysis also indicates that even after the storm has passed, some areas (as seen in Run-F) remain underwater. This residual flooding is attributed to the overtopping of seawalls, which act as barriers preventing the seawater from receding. This insight points to a need for reconsideration of coastal defenses, such as seawalls, to ensure they facilitate the effective drainage of floodwaters post-storm.

By taking into account the inundation depth in addition to the inundation area, we can calculate the time series of inundation volume, as illustrated in Figure 9b. The interaction between tides and storm surges—referred to as tide-surge interaction—has a significant effect on the inundation volume. The peak inundation volume can be reduced from approximately 3.56×10^7 m^3 to around 1.23×10^7 m^3. About 2/3 inundation volume during the peak inundation moment are reduced by the tide-surge interaction.

4 Discussion

4.1 Understanding the characteristics of tide-surge interaction

The most remarkable feature of a typhoon is the high winds. Consider a simple situation of a 1-D flow with constant wind field described by (Pugh, 1987), where the barotropic force is in equilibrium with the surface wind force. We can derive a simplified expression

$$\frac{\partial \zeta}{\partial x} = \frac{C_d \rho_a U^2}{g \rho D} \tag{10}$$

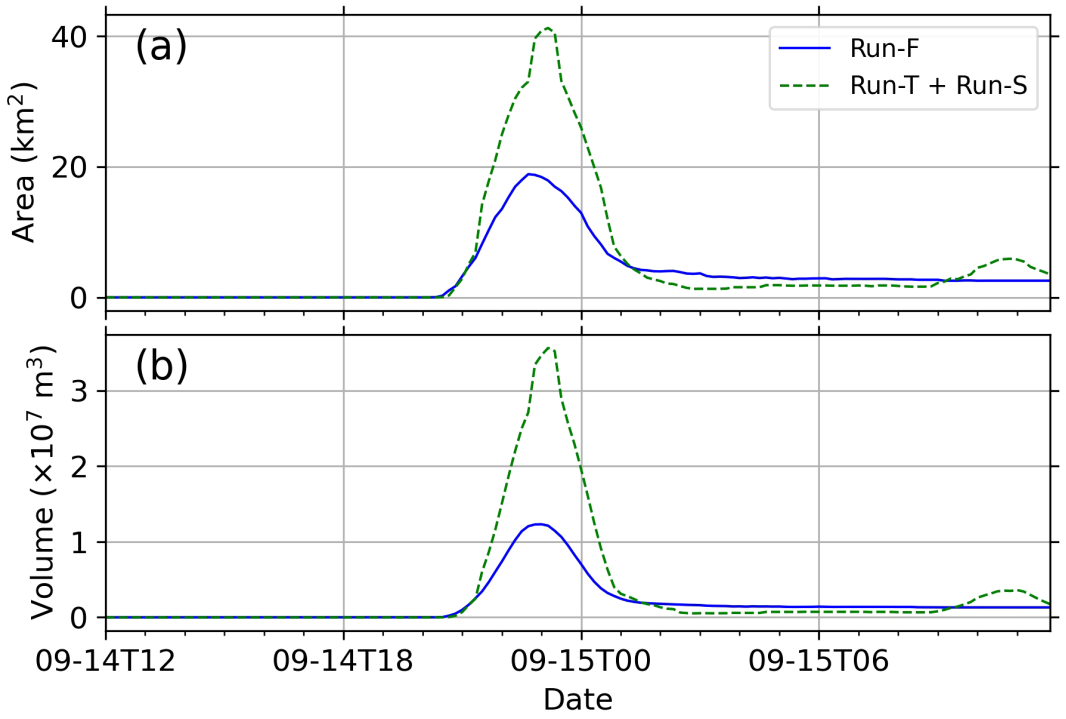

FIGURE 9
Time series of **(A)** inundation area, and **(B)** inundation volumes in Xiamen Bay. Only positions with height > 3.0 m are included. The solid blue lines represent results from Run-F and the dashed green lines indicate the results deduced from the summation of Run-T and Run-S.

where C_d is the surface drag coefficient, ρ_a and ρ are the densities of air and water, respectively, U is the surface wind speed, and D is the total water depth.

This formula provides a clear interpretation of the tidal modulation effects on surges. Wind-driven surges tend to be smaller during periods of deeper water depth at high tide, but significantly larger at low tide. This effect is particularly pronounced in shallow waters, where the total water depth can undergo significant changes between high tide and low tide (Idier et al., 2019; Zhang et al., 2017). During Typhoon Meranti, observations from the Xiamen tidal gauge (Figure 4) and results from our model both indicate a non-negligible reduction in the practical surge height during high tide (Figure 6), which can be readily explained by Equation 10.

It is widely believed that a positive surge will accelerate the propagation of tides, and vice versa (Prandle and Wolf, 1978; Rossiter, 1961). In conjunction with changes in bottom friction, tidal amplitudes during storms are considered to differ from those of astronomical tides, as analyzed by Feng et al. (2016). Thus, the surge levels can be expressed as:

$$R = TS - T = Bcos(\omega t + \varphi) - Acos(\omega t) = \hat{A}\cos(\omega t + \theta) \quad (11)$$

where B is the observed tidal amplitude during a storm, A is the astronomical tidal amplitude, φ is the phase shift of the tide caused by the storm, $\varphi > 0$ indicates that the tide is advanced by the storm. Equation 11 clearly reveals that a tidal period will be present in the surges, which corresponds with the two-peaks feature depicted in Figure 6.

If we define α to be the scale of tidal amplitude reduction/amplification, that is, $B = (1 - \alpha) A$, the amplitude and phase of surge amplitude can then be expressed as:

$$\begin{aligned}\hat{A} &= \sqrt{(A - B\cos\varphi)^2 + (B\sin\varphi)^2} \\ &= A\sqrt{1 - 2(1-\alpha)\cos\varphi + (1-\alpha)^2} \\ &= A\sqrt{2(1-\alpha)(1-\cos\varphi) + \alpha^2} \\ &= A\sqrt{[\alpha - (1-\cos\varphi)]^2 + 1 - cos^2\varphi}\end{aligned} \quad (12)$$

$$\theta = arctan\frac{B\sin\varphi}{B\cos\varphi - A} = arctan\frac{(1-\alpha)\sin\varphi}{(1-\alpha)\cos\varphi - 1} \quad (13)$$

For a given α, a phase advance or delay will lead to the same surge amplitude, since $\cos\varphi$ is an even function. According to Equation 12, for a given φ, the surge amplitude reaches its minimum $A|\sin\varphi|$ when $\alpha = 1 - \cos\varphi$. For a small α and a relatively significant phase shift φ, we can have a quick assessment of the surge amplitude with $\hat{A} \approx 2\sqrt{1-\alpha}\left|sin\frac{\varphi}{2}\right|A$. Thus, if we ignore the amplitude modulation in tide, i.e., $\alpha = 0$, the surge amplitude can be estimated as:

$$\hat{A} = 2\left|sin\frac{\varphi}{2}\right|A \quad (14)$$

and the surge phase can be assessed through set α=0 in Equation 13:

$$\theta = arctan\frac{\sin\varphi}{\cos\varphi - 1} = arctan\frac{\cos\frac{\varphi}{2}}{-\sin\frac{\varphi}{2}} = \frac{\varphi}{2} + \frac{\pi}{2} + k\pi \quad (15)$$

According to Equations 14 and 15, if the phase shift is also small, this means the phase of surge is nearly in quadrature with the tidal phase. This implies that a peak of surge tends to occur around mid-rising tide or mid-falling tide due to tide-surge interaction, which coincides with the practical surges (ζ_{SI}) displayed in Figure 6. And the latter peaks occurring around mid-falling tide in Figure 6 are the combined effect of the strong winds induced pure surges and tide-surge interactions, which are demonstrated by the pure surges (ζ_S). This highlights the important role of tide-surge interaction in the double-peak feature of the practical surges.

4.2 Contribution of nonlinear interactions

Tide-surge interaction primarily arises from three nonlinear terms: advection, bottom friction, and shallow water effect, which is due to $D = H + \zeta$. The most widely-used method to determine the contribution of these three nonlinear physical processes is to conduct numerical experiments, in which each nonlinear process is either linearized or removed (Bernier and Thompson, 2007; Zhang et al., 2017). Idier et al. (2012) and Zheng et al. (2020) proposed an inverse approach by comparing a baseline experiment, which excludes all three nonlinear processes, with experiments that include only one nonlinear effect at a time. Yang et al. (2019) suggested a method to establish a direct relationship between the nonlinear tide-surge interaction and each term in the momentum equation (Appendix A).

Following the method proposed by Yang et al. (2019), the residual momentum terms resulting from tide-surge interaction, including the nonlinear local acceleration term $\frac{\partial U_I}{\partial t}$ and $\frac{\partial V_I}{\partial t}$ (ACC), the nonlinear advection term ψ_x and ψ_y (ADV), the nonlinear Coriolis force term $-fV_I$ and fU_I (COR), and nonlinear surface wind and bottom friction term τ_x^I, τ_y^I (FSB) at the four representative stations shown in Figure 1b are displayed in Figure 10. The results indicate that the ACC and ADV terms are significant at all four stations, suggesting that these terms play dominant roles in controlling the nonlinear interaction throughout Xiamen Bay. The residual magnitudes, particularly around Dadeng Island (P3), are notably high (exceeding 1×10^3 m/s^2), indicating an exceptionally strong nonlinear tide-surge interaction in this area. However, the ζ_I at P3 are not the most significant among the four stations (refer to Figure 6). This result implies that ζ_I is not a consequence of local tide-surge interaction, but rather relates to the cumulative nonlinear interaction from a wider area.

Nevertheless, in the Jiulong River Estuary (P2) and around Dadeng Island (P3), where the waters are shallow, the FSB terms are also prominent in both x and y-directions. This characteristic is consistent with the numerical results found in Tieshan Bay, China (Yang et al., 2019), and in macro-tidal Hangzhou Bay (Li et al., 2022). It can be attributed to the intensification of tidal current, which in turn strengthens the advection and bottom friction terms.

5 Conclusions

In this study, a high-resolution numerical model based on FVCOM has been established to cover the coastal low-lying land

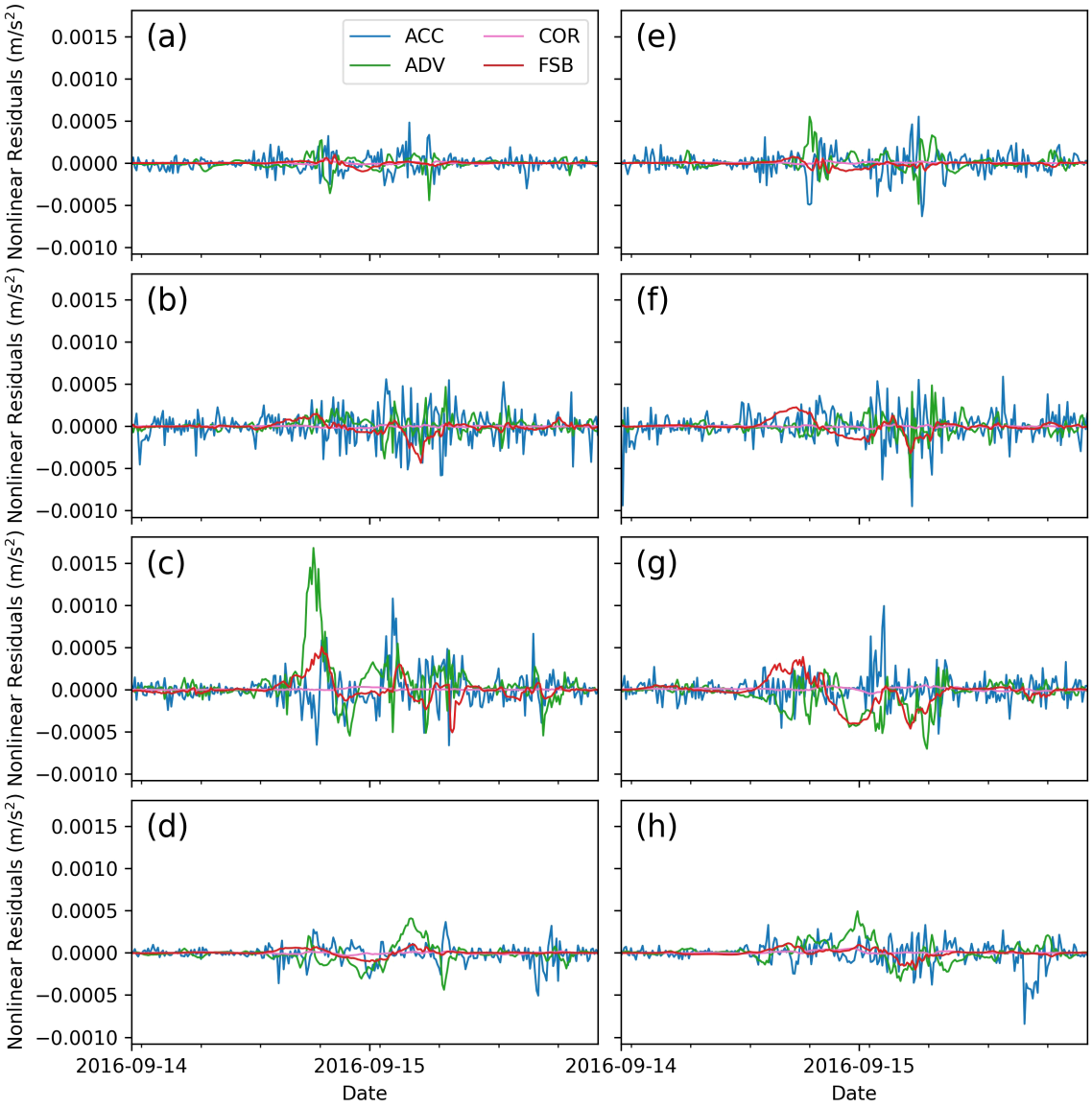

FIGURE 10
Time series of nonlinear components for representative stations. **(A–C)**, and **(D)** are the nonlinear components of x direction at P1, P2, P3 and P4, respectively; and **(E–H)** are those at y direction. The positions of the four stations are indicated in Figure 1b.

in Xiamen Bay, China. Super Typhoon Meranti (1614) is used as a case study to investigate the tide-surge interaction and its impact on coastal inundation. According to the numerical results, we obtain conclusions as follows:

1. Nonlinear tide-surge interaction modulates extreme sea levels and surges in different patterns.

   Our numerical results indicate that the tide-surge interaction is extremely strong in Xiamen Bay. It's relative intensity to the practical surges can be larger than 0.3 across most area of the bay. Tide-surge interaction tends to lower extreme sea levels throughout Xiamen Bay during Meranti. However, the nonlinear interaction elevates peak surges in Weitou Bay, around Dadeng Island and in Tong'an Bay, but reduce surges in the Jiulong Estuary and around the Xiaojinmen Island.
2. Double-peak pattern in storm tides can mainly attributed to the strong tide-surge interaction.

   A pronounced double-peak feature is evident in the nonlinear surges, with peaks occurring at mid-rising and mid-falling tide. We demonstrate that the mid-rising peak in storm tides can mainly attribute to the nonlinear tide-surge interaction, and the mid-falling peak is the result combining the direct effect of strong wind and tide-surge interaction.
3. The nonlinear tide-surge interaction primarily results from the nonlinear transformations in local acceleration term and advection term.

The momentum balance analysis indicates that local acceleration term and advection term are significant across the whole Xiamen Bay. Whereas, in the Jiulong River Estuary and around Dadeng Island where the waters are shallow, the nonlinear surface wind and bottom frictions are also prominent, showing the contribution of intensification of tidal current in shallow waters, which can in turn enhances the advection and bottom frictions.

4. Tide-surge interaction can significantly weaken coastal inundation hazards.

As a result of tide-surge interaction, which induces lower extreme sea levels, the inundation areas, inundation depths, and inundation durations in Xiamen Bay are also reduced, by approximately 24%, 16%, and 10%, respectively. In some coastal corner zones, the impacts may differ, reflecting the effects of complex coastlines. These variations should be carefully considered when implementing coastal management strategies.

On the context of global warming, the extreme sea levels are expected to be raised-up along with global sea level rise, exacerbating coastal inundation. Many studies demonstrated the important role of nonlinear tide-surge interaction on coastal inundation (Lyddon et al., 2018; Xiao et al., 2021). However, many large-scale assessment of coastal inundation ignored the nonlinear tide-surge interaction (e.g., Hauer et al., 2021). This study offers a reference that how much errors may lie in those assessment. In addition, the progress in the understanding of tide-surge interaction in this study may motivate methodological development in quantifying tide-surge interaction across regions, which was regarded as one important factor hampers the estimation of tide-surge interactions (Arns et al., 2020).

Data availability statement

The raw data supporting the conclusions of this article will be made available by the authors, without undue reservation.

Author contributions

WG: Conceptualization, Funding acquisition, Methodology, Writing – original draft, Writing – review & editing. FZ: Data curation, Validation, Visualization, Writing – original draft. JG: Conceptualization, Resources, Supervision, Writing – review & editing. HZ: Conceptualization, Funding acquisition, Supervision, Writing – review & editing.

Funding

The author(s) declare that financial support was received for the research, authorship, and/or publication of this article. This work is supported by National Natural Science Foundation of China (Grant No. 41906143) and Shanghai Sailing Program (Grant No. 19YF1418500). The authors WG and HZ are also supported by Shanghai Frontiers Science Center of "Full Penetration" Far-Reaching Offshore Ocean Energy and Power.

Acknowledgments

The authors thank Fujian Provincial Department of Ocean and Fisheries very much for offering of the datasets used in this study, including the naval electric nautical charts, land topography, seawall locations and heights, observed tidal levels during tropical cyclones, and so on. The first author WG expresses his appreciation to Shanghai Maritime University for offering a high- performance supercomputer where all the simulations are conducted on.

Conflict of interest

The authors declare that the research was conducted in the absence of any commercial or financial relationships that could be construed as a potential conflict of interest.

Generative AI statement

The author(s) declare that no Generative AI was used in the creation of this manuscript.

Publisher's note

References

Aðalgeirsdóttir, G., Drijfhout, S. S., Edwards, T. L., Golledge, N. R., Hemer, M., Kopp, R. E., et al. (2021). "Ocean, Cryosphere and Sea Level Change," in *Climate Change 2021: The Physical Science Basis. Contribution of Working Group I to the Sixth Assessment Report of the Intergovernmental Panel on Climate Change*. Eds. D. Masson, V. P. Zhai, A. Pirani, S. L. Connors, C. Pean, S. Berger, N. Caud, Y. Chen, L. Goldfarb, M. I. Gomis, M. Huang, K. Leitzell, E. Lonnoy, J. B. R. Matthews, T. K. Maycock, T. Waterfield, O. Yelekci, R. Yu and B. Zhou (Cambridge University Press, Cambridge, United Kingdom and New York, NY, USA), 1211–1362.

Amante, C., and Eakins, B. W. (2009). ETOPO1 1 arc-minute global relief model: Procedures, data sources and analysis. *NOAA Technical Memorandum NESDIS NGDC-24*. National Geophysical Data Center, NOAA.

Antony, C., Unnikrishnan, A. S., Krien, Y., Murty, P. L. N., Samiksha, S. V., and Islam, A. K. M. S. (2020). Tide–surge interaction at the head of the bay of bengal during cyclone aila. *Regional Stud. Mar. Science.* 35, 101133. doi: 10.1016/j.rsma.2020.101133

Arns, A., Wahl, T., Wolff, C., Vafeidis, A. T., Haigh, I. D., Woodworth, P., et al. (2020). Non-linear interaction modulates global extreme sea levels, coastal flood exposure, and impacts. *Nat. Commun.* 11, 1918. doi: 10.1038/s41467-020-15752-5

As-salek, J. A., and Yasuda, T. (2001). Tide-surge interaction in the meghna estuary: most severe conditions. *J. Phys. Oceanography.* 31, 3059–3072. doi: 10.1175/1520-0485(2001)031<3059:TSIITM>2.0.CO;2

Bernier, N. B., and Thompson, K. R. (2007). Tide-surge interaction off the east coast of Canada and northeastern United States. *J. Geophys. Res.* 112. doi: 10.1029/2006JC003793

Chen, C., Beardsley, R. C., and Cowles, G. (2013). An unstructured grid, finite-volume coastal ocean model: fvcom user manual, new bedford.

Chen, C., Liu, H., and Beardsley, R. C. (2003). An unstructured grid, finite-volume, three-dimensional, primitive equations ocean model: application to coastal ocean and estuaries. *J. Atmospheric Oceanic Technology.* 20, 159–186. doi: 10.1175/1520-0426(2003)020<0159:AUGFVT>2.0.CO;2

Cruse, G. (2020). *Impact of Flooding On Power System Restoration Following a Hurricane.* Pittsburgh: University of Pittsburgh.

Dong, Y., Zheng, Z., Ma, Y., Gao, J., Ma, X., and Dong, G. (2023). Numerical investigation on the mitigation of harbor oscillations by periodic undulating topography. *Ocean Engineering.* 279, 114580. doi: 10.1016/j.oceaneng.2023.114580

Egbert, G. D., and Erofeeva, S. Y. (2002). Efficient inverse modeling of barotropic ocean tides. *J. Atmospheric Oceanic Technology.* 19, 183–204. doi: 10.1175/1520-0426(2002)019<0183:EIMOBO>2.0.CO;2

Elahi, M. W. E., Wang, X. H., Salcedo-Castro, J., and Ritchie, E. A. (2023). Influence of wave–current interaction on a cyclone-induced storm surge event in the ganges–brahmaputra–meghna delta: part 1—Effects on water level. *Jmse* 11, 328. doi: 10.3390/jmse11020328

Feng, Y., Brubaker, K. L., and McCuen, R. H. (2017). New view of flood frequency incorporating duration. *J. Hydrologic Engineering.* 22, 4017051. doi: 10.1061/(ASCE)HE.1943-5584.0001573

Feng, J., Jiang, W., Li, D., Liu, Q., Wang, H., and Liu, K. (2019). Characteristics of tide–surge interaction and its roles in the distribution of surge residuals along the coast of China. *J. Oceanography.* 75, 225–234. doi: 10.1007/s10872-018-0495-8

Feng, X., Olabarrieta, M., and Valle-Levinson, A. (2016). Storm-induced semidiurnal perturbations to surges on the us eastern seaboard. *Continental Shelf Res.* 114, 54–71. doi: 10.1016/j.csr.2015.12.006

Fujita, T. (1952). Pressure distribution within typhoon. *Geophys. Mag.* 23, 437–451.

Gao, J., Hou, L., Liu, Y., and Shi, H. (2024). Influences of bragg reflection on harbor resonance triggered by irregular wave groups. *Ocean Engineering.* 305, 117941. doi: 10.1016/j.oceaneng.2024.117941

Gao, J., Ma, X., Dong, G., Chen, H., Liu, Q., and Zang, J. (2021). Investigation on the effects of bragg reflection on harbor oscillations. *Coast. Engineering.* 170, 103977. doi: 10.1016/j.coastaleng.2021.103977

Guo, W., Yao, D., Chen, Z., Ding, P., and Ge, J. (2023). Assessment of future flood risk induced by sea level rise and tropical cyclones under global warming in the xiamen bay, fujian, China. *Front. Mar. Sci.* 10. doi: 10.3389/fmars.2023.1103279

Hauer, M. E., Hardy, D., Kulp, S. A., Mueller, V., Wrathall, D. J., and Clark, P. U. (2021). Assessing population exposure to coastal flooding due to sea level rise. *Nat. Commun.* 12. doi: 10.1038/s41467-021-27260-1

He, Z., Tang, Y., Xia, Y., Chen, B., Xu, J., Yu, Z., et al. (2020). Interaction impacts of tides, waves and winds on storm surge in a channel-island system: observational and numerical study in yangshan harbor. *Ocean Dynamics.* 70, 307–325. doi: 10.1007/s10236-019-01328-5

Hersbach, H., Bell, B., Berrisford, P., Hirahara, S., Horányi, A., Muñoz Sabater, J., et al. (2020). The era5 global reanalysis. *Q.J.R. Meteorol. Soc* 146, 1999–2049. doi: 10.1002/qj.v146.730

Horsburgh, K. J., and Wilson, C. (2007). Tide-surge interaction and its role in the distribution of surge residuals in the north sea. *J. Geophys. Res.* 112. doi: 10.1029/2006JC004033

Huang, Y., Yang, H., Wang, Y. P., Jia, J., Wang, Z., Zhu, Q., et al. (2022). Swell-driven sediment resuspension in the yangtze estuary during tropical cyclone events. *Estuarine Coast. Shelf Science.* 267, 107765. doi: 10.1016/j.ecss.2022.107765

Idier, D., Bertin, X., Thompson, P., and Pickering, M. D. (2019). Interactions between mean sea level, tide, surge, waves and flooding: mechanisms and contributions to sea level variations at the coast. *Surveys Geophysics.* 40, 1603–1630. doi: 10.1007/s10712-019-09549-5

Idier, D., Dumas, F., and Muller, H. (2012). Tide-surge interaction in the english channel. *Natural Hazards Earth System Sci.* 12, 3709–3718. doi: 10.5194/nhess-12-3709-2012

Johns, B., Rao, A. D., Dubinsky, Z., Sinha, P. C., and Lighthill, M. J. (1985). Numerical modelling of tide-surge interaction in the bay of bengal. *Philos. Trans. R. Soc. London. Ser. Math. Phys. Sci.* 313 (1526), 507–535. doi: 10.1098/rsta.1985.0002

Large, W. G., and Pond, S. (1981). Open ocean momentum flux measurements in moderate to strong winds. *J. Phys. Oceanography.* 11, 324–336. doi: 10.1175/1520-0485(1981)011<0324:OOMFMI>2.0.CO;2

Li, C. (2006). Modeling of bathymetry-locked residual eddies in well-mixed tidal channels with arbitrary depth variations. *J. Phys. Oceanography.* 36, 1974–1993. doi: 10.1175/JPO2955.1

Li, C., Chen, C., Guadagnoli, D., and Georgiou, I. Y. (2008). Geometry-induced residual eddies in estuaries with curved channels: observations and modeling studies. *J. Geophys. Res.* 113. doi: 10.1029/2006JC004031

Li, L., Li, Z., He, Z., Yu, Z., and Ren, Y. (2022). Investigation of storm tides induced by super typhoon in macro-tidal hangzhou bay. *Front. Mar. Sci.* 9. doi: 10.3389/fmars.2022.890285

Liu, W., Huang, W., and Chen, W. (2016). Modeling the interaction between tides and storm surges for the Taiwan coast. *Environ. Fluid Mechanics.* 16, 721–745. doi: 10.1007/s10652-015-9441-0

Lyddon, C., Brown, J. M., Leonardi, N., and Plater, A. J. (2018). Flood hazard assessment for a hyper-tidal estuary as a function of tide-surge-morphology interaction. *Estuaries Coasts.* 41, 1565–1586. doi: 10.1007/s12237-018-0384-9

Miao, Q., Yue, X., Yang, J., Wang, Z., Xu, S., Yang, Y., et al. (2022). Characteristics analysis and risk assessment of extreme water levels based on 60-year observation data in xiamen, China. *J. Ocean Univ. China.* 21, 315–322. doi: 10.1007/s11802-022-4844-2

Miyazaki, M. T. U. (1962). Theoretical investigations of typhoon surges along the Japanese coast (I). *Oceanographic Magazine.* 13, 353–354.

Peng, S., and Li, Y. (2015). A parabolic model of drag coefficient for storm surge simulation in the south China sea. *Sci. Rep.* 5, 1–6. doi: 10.1038/srep15496

Pinheiro, J. P., Lopes, C. L., Ribeiro, A. S., Sousa, M. C., and Dias, J. M. (2020). Tide-surge interaction in ria de aveiro lagoon and its influence in local inundation patterns. *Continental Shelf Res.* 200, 104132. doi: 10.1016/j.csr.2020.104132

Prandle, D., and Wolf, J. (1978). The interaction of surge and tide in the north sea and river thames. *Geophysical J. Int.* 55, 203–216. doi: 10.1111/j.1365-246X.1978.tb04758.x

Proudman, J. (1955). The propagation of tide and surge in an estuary. *Proc. R. Soc. London. Ser. a. Math. Phys. Sci.* 231 (1184), 8–24. doi: 10.1098/rspa.1955.0153

Pugh, D. T. (1987). *Tides, surges and Mean Sea-Level: A Handbook for Engineers and Scientists* Vol. 472 (Hoboken, NJ: John Wiley).

Pyatkova, K., Chen, A. S., Butler, D., Vojinović, Z., and Djordjević, S. (2019). Assessing the knock-on effects of flooding on road transportation. *J. Environ. Management.* 244, 48–60. doi: 10.1016/j.jenvman.2019.05.013

Quinn, N., Atkinson, P. M., and Wells, N. C. (2012). Modelling of tide and surge elevations in the solent and surrounding waters: the importance of tide–surge interactions. *Estuarine Coast. Shelf Science.* 112, 162–172. doi: 10.1016/j.ecss.2012.07.011

Rego, J. L., and Li, C. (2010). Nonlinear terms in storm surge predictions: effect of tide and shelf geometry with case study from hurricane rita. *J. Geophys. Res.: Oceans* 115 (C6). doi: 10.1029/2009JC005285

Rossiter, J. R. (1961). Interaction between tide and surge in the thames. *Geophysical J. Int.* 6, 29–53. doi: 10.1111/j.1365-246X.1961.tb02960.x

Song, H., Kuang, C., Gu, J., Zou, Q., Liang, H., Sun, X., et al. (2020). Nonlinear tide-surge-wave interaction at a shallow coast with large scale sequential harbor constructions. *Estuarine Coast. Shelf Science.* 233, 106543. doi: 10.1016/j.ecss.2019.106543

Tang, Y. M., Grimshaw, R., Sanderson, B., and Holland, G. (1996). A numerical study of storm surges and tides, with application to the north queensland coast. *J. Phys. Oceanography.* 26, 2700–2711. doi: 10.1175/1520-0485(1996)026<2700:ANSOSS>2.0.CO;2

Thomas, A., Dietrich, J. C., Dawson, C. N., and Luettich, R. A. (2022). Effects of model resolution and coverage on storm-driven coastal flooding predictions. *J. Waterway Port Coastal Ocean Engineering.* 148, 4021046. doi: 10.1061/(ASCE)WW.1943-5460.0000687

Wagnaar, D. (2012). *The significance of Flood Duration for Flood Damage Assessment* (Delft: Delft University of Technology-Deltares).

Willmott, C. J. (1981). On the validation of models. *Phys. Geography.* 2, 184–194. doi: 10.1080/02723646.1981.10642213

Wolf, J. (1981). "Surge-Tide Interaction in the North Sea and River Thames" in the *Floods Due to High Winds and Tides,* ed. D. H. Peregrine (London: Academic), 75–94.

Xiao, Z., Yang, Z., Wang, T., Sun, N., Wigmosta, M., and Judi, D. (2021). Characterizing the non-linear interactions between tide, storm surge, and river flow in the delaware bay estuary, United States. *Front. Mar. Sci.* 8. doi: 10.3389/fmars.2021.715557

Yang, W., Yin, B., Feng, X., Yang, D., Gao, G., and Chen, H. (2019). The effect of nonlinear factors on tide-surge interaction: A case study of typhoon rammasun in tieshan bay, China. *Estuarine Coast. Shelf Science.* 219, 420–428. doi: 10.1016/j.ecss.2019.01.024

Yu, X., Pan, W., Zheng, X., Zhou, S., and Tao, X. (2017). Effects of wave-current interaction on storm surge in the Taiwan strait: insights from typhoon morakot. *Continental Shelf Res.* 146, 47–57. doi: 10.1016/j.csr.2017.08.009

Yuan, F., Zhang, W., Ye, Y., and Zhang, S. (2022). The storm surge inundation risk warning system for xiamen. *Mar. Dev. Management.* (4), 102–106. doi: 10.20016/j.cnki.hykfygl.20220330.017

Zhang, H., Cheng, W., Qiu, X., Feng, X., and Gong, W. (2017). Tide-surge interaction along the east coast of the leizhou peninsula, south China sea. *Continental Shelf Res.* 142, 32–49. doi: 10.1016/j.csr.2017.05.015

Zhang, W., Shi, F., Hong, H., Shang, S., and Kirby, J. T. (2010). Tide-surge interaction intensified by the Taiwan strait. *J. Geophys. Res.* 115. doi: 10.1029/2009JC005762

Zhang, W., Villarini, G., Vecchi, G. A., and Smith, J. A. (2018). Urbanization exacerbated the rainfall and flooding caused by hurricane harvey in houston. *Nature* 563, 384–388. doi: 10.1038/s41586-018-0676-z

Zheng, P., Li, M., Wang, C., Wolf, J., Chen, X., De Dominicis, M., et al. (2020). Tide-surge interaction in the pearl river estuary: A case study of typhoon hato. *Front. Mar. Sci.* 7. doi: 10.3389/fmars.2020.00236

Appendix A

In this section, we analyze the momentum balance in Run-F, Run-T and Run-S. To streamline the discussion, diffusion terms are excluded. In Run-F, which considers both tides and surface wind stresses, the momentum equations can be formulated as follows:

$$\frac{\partial U_{TS}}{\partial t} + U_{TS}\frac{\partial}{\partial x}U_{TS} + V_{TS}\frac{\partial}{\partial y}U_{TS} - fV_{TS} = -g\frac{\partial \zeta_{TS}}{\partial x} + \frac{\partial P_S}{\rho_O \partial x} + \frac{\tau_{sx} - \tau_{bx}^{TS}}{(h+\zeta_{TS})\rho_0}, \tag{A1}$$

$$\frac{\partial V_{TS}}{\partial t} + U_{TS}\frac{\partial}{\partial x}V_{TS} + V_{TS}\frac{\partial}{\partial y}V_{TS} + fU_{TS} = -g\frac{\partial \zeta_{TS}}{\partial y} + \frac{\partial P_S}{\rho_O \partial y} + \frac{\tau_{sy} - \tau_{by}^{TS}}{(h+\zeta_{TS})\rho_0}, \tag{A2}$$

For Run-T, which only considers astronomical tidal forcing, the momentum equations are expressed as:

$$\frac{\partial U_T}{\partial t} + U_T\frac{\partial}{\partial x}U_T + V_T\frac{\partial}{\partial y}U_T - fV_T = -g\frac{\partial \zeta_T}{\partial x} - \frac{\tau_{bx}^{T}}{(h+\zeta_T)\rho_0}, \tag{A3}$$

$$\frac{\partial V_T}{\partial t} + U_T\frac{\partial}{\partial x}V_T + V_T\frac{\partial}{\partial y}V_T + fU_T = -g\frac{\partial \zeta_T}{\partial y} - \frac{\tau_{by}^{T}}{(h+\zeta_T)\rho_0}, \tag{A4}$$

In Run-S, which only considers the surface wind stress, the momentum equations are:

$$\frac{\partial U_S}{\partial t} + U_S\frac{\partial}{\partial x}U_S + V_S\frac{\partial}{\partial y}U_S - fV_S = -g\frac{\partial \zeta_S}{\partial x} + \frac{\partial P_S}{\rho_O \partial x} + \frac{\tau_{sx} - \tau_{bx}^{S}}{(h+\zeta_S)\rho_0}, \tag{A5}$$

$$\frac{\partial V_S}{\partial t} + U_S\frac{\partial}{\partial x}V_S + V_S\frac{\partial}{\partial y}V_S + fU_S = -g\frac{\partial \zeta_S}{\partial y} + \frac{\partial P_S}{\rho_O \partial y} + \frac{\tau_{sy} - \tau_{by}^{S}}{(h+\zeta_S)\rho_0}, \tag{A6}$$

Hence, the momentum equations for tide-surge interaction can be derived by combining Equation A1 – Equation A3 – Equation A5 in the x direction, and Equation A2 – Equation A4 – Equation A6 in the y direction. The results are:

$$\frac{\partial U_I}{\partial t} + \psi_x(U_I, V_I) - fV_I - \tau_x^I = -g\frac{\partial \zeta_I}{\partial x}, \tag{A7}$$

$$\frac{\partial V_I}{\partial t} + \psi_y(U_I, V_I) + fU_I - \tau_y^I = -g\frac{\partial \zeta_I}{\partial y} \tag{A8}$$

where

$$U_I = U_{TS} - U_T - U_S, \tag{A9}$$

$$V_I = V_{TS} - V_T - V_S, \tag{A10}$$

$$\psi_x(U_I, V_I) = U_{TS}\frac{\partial}{\partial x}U_{TS} + V_{TS}\frac{\partial}{\partial y}U_{TS} - U_T\frac{\partial}{\partial x}U_T - V_T\frac{\partial}{\partial y}U_T - U_S\frac{\partial}{\partial x}U_S - V_S\frac{\partial}{\partial y}U_S, \tag{A11}$$

$$\psi_y(U_I, V_I) = U_{TS}\frac{\partial}{\partial x}V_{TS} + V_{TS}\frac{\partial}{\partial y}V_{TS} - U_T\frac{\partial}{\partial x}V_T - V_T\frac{\partial}{\partial y}V_T - U_S\frac{\partial}{\partial x}V_S - V_S\frac{\partial}{\partial y}V_S, \tag{A12}$$

$$\tau_x^I = \frac{\tau_{sx} - \tau_{bx}^{TS}}{(h+\zeta_{TS})\rho_0} + \frac{\tau_{bx}^{T}}{(h+\zeta_T)\rho_0} - \frac{\tau_{sx} - \tau_{bx}^{S}}{(h+\zeta_S)\rho_0}, \tag{A13}$$

$$\tau_y^I = \frac{\tau_{sy} - \tau_{by}^{TS}}{(h+\zeta_{TS})\rho_0} + \frac{\tau_{by}^{T}}{(h+\zeta_T)\rho_0} - \frac{\tau_{sy} - \tau_{by}^{S}}{(h+\zeta_S)\rho_0}, \tag{A14}$$

In Equations A7–A14, (U_I, V_I) represents the residual current components in the x and y directions due to tide-surge interaction, the terms $\psi_x(U_I, V_I)$ and $\psi_y(U_I, V_I)$ denote the residual advection terms associated with tide-surge interaction, $(-fV_I, fU_I)$ represents the residual Coriolis force related to tide-surge interaction, and (τ_x^I, τ_y^I) defines the residual of wind stress and bottom friction terms due to tide-surge interaction.